Characterization of the acquisition modes implemented in Pixirad-1/Pixie-III X-ray Detector: Effects of charge sharing correction on spectral resolution and image quality

V. Di Trapani [a,b,*], A. Bravin [c], F. Brun [d,e], D. Dreossi [f], R. Longo [e,g], A. Mittone [h], L. Rigon [e,g], P. Delogu [a,b]

[a] Dipartimento di Scienze Fisiche, della Terra e dell'Ambiente, Università di Siena, Presidio San Niccolò, Via Roma 56, I-53100, Italy
[b] INFN - Sezione di Pisa, Largo B. Pontecorvo 3, Pisa, I-56127, Italy
[c] European Synchrotron Radiation Facility, avenue des Martyrs 71, Grenoble, France
[d] Dipartimento di Ingegneria e Architettura, Università di Trieste, Via A. Valerio, 6/1 – Trieste, I-34127, Italy
[e] INFN - Sezione di Trieste, Via A. Valerio 2, Trieste, I-34127, Italy
[f] Elettra-Sincrotrone Trieste S.C.p.A, s.s. 14-km 163.5 in Area Science Park, Basovizza, Trieste, I-34149, Italy
[g] Dipartimento di Fisica, Università di Trieste, Via A. Valerio 2, Trieste, I-34127, Italy
[h] CELLS - ALBA synchrotron light source, Carrer de la Llum, 2-26, 08290 Cerdanyola del Vallès, Barcelona, Spain

ARTICLE INFO

Keywords:
X-ray photon counting detectors
Spectral imagers
Charge sharing
Multiple counts

ABSTRACT

X-ray Photon Counting Detectors (XPCDs) with thick semiconductor sensors and small pixel sizes suffer from a charge-sharing effect which can induce multiple counts from a single interacting photon. This issue degrades not only the energy resolution, but it also worsens the spatial resolution. Multiple counts can be removed by acting on the discriminator threshold or they can be corrected by means of specific acquisition modalities implemented in the readout electronics. In this paper we present the results of the characterization of the Pixirad-1/Pixie-III device, a XPCD carrying a 650 μm thick CdTe sensor with a small pixel (62×62 μm^2). The Pixie-III readout system includes programmable energy thresholds and it implements three acquisition modes: a pure photon counting mode and two modes specially designed to correct charge-sharing effects. The measured energy resolution of the three acquisition modes for different energies are here reported. Moreover, we characterize the imaging performance for different combinations of acquisition modes and thresholds by measuring the presampling Modulation Transfer Function (MTF), the Normalized Noise Power Spectrum (NNPS) and by assessing the Noise Equivalent number of Quanta (NEQ).

1. Introduction

Large area X-ray Photon Counting Detectors (XPCD) are of great interest in medical imaging [1,2], due to their high detection efficiency and low intrinsic noise, which allow overcoming the main limitations of the charge integrating devices. These imaging detectors are now available with pixel sizes in the range of 50–70 μm; all these characteristics make them suitable for a broad range of applications, from material science to biomedicine. For instance, XPCDs are attractive for low dose imaging applications; and they have been already employed in mammography and breast computed tomography in both commercial systems [3,4] and experimental setups [5–7].

By implementing one or more programmable energy thresholds, a XPCD is able to remove the electronic noise and to discriminate the impinging photons according to their energy, thus making them suitable also for spectral applications such as the K-Edge Subtraction (KES) imaging. This technique exploits the sharp raise of the linear attenuation coefficients at the K-edge of high-Z elements (contrast agents) embedded into injectable pharmaceuticals. In particular, when imaging with a polychromatic source, a XPCD allows the simultaneous acquisition of two images with energy bins below and above the K-edge of the high Z element. The subtraction of these two images enhances the presence of the contrast agent in anatomical structures of interest [8,9].

Hybrid XPCDs are made by coupling a thick semiconductor sensor (such as e.g. Si, Ge, CdTe, CdZnTe crystals) with the readout electronics, however the charge produced in the active area by an interacting X-ray photon can be spread over neighboring pixels. This effect, called charge sharing, occurs for each combination of sensor material and thickness, but it is enhanced when the thickness-to-pixel size ratio increases. When charge sharing occurs, multiple counts from a single

* Corresponding author at: INFN - Sezione di Pisa, Largo B. Pontecorvo 3, Pisa, I-56127, Italy.
E-mail address: vittorio.ditrapani@pi.infn.it (V. Di Trapani).

interacting photon can be induced, thus degrading both the spectral and spatial resolution [10–17].

For monochromatic radiation, by using a pure counting mode, i.e. without specific corrections for charge sharing, multiple counts can be partially or totally removed by properly tuning the discrimination threshold *Thr*. For instance, when monochromatic photons with energy E are employed, multiple counts are detected if $Thr < E/2$, while for $Thr > E/2$ some events are lost with a consequent decrease of the detection efficiency [10,18]. To remove multiple counts by limiting the loss of efficiency, *Thr* has to be set to $E/2$ [10,19,20]. However, the removal of multiple counts does not solve the degradation of the energy resolution, thus different solutions have been proposed to correct for charge-sharing effect. Solutions proposed in literature include (i) changing the pixel geometry (e.g. using hexagonal pixels instead of square pixels [21]), (ii) the reduction of the charge collection time by operating with high bias voltages [22] and (iii) the implementation of specifically designed algorithms for charge sharing suppression in the readout systems [21,23–26]. These algorithms trace back the energy deposited by a single photon by summing the charge collected in a cluster of (3 up to 8) pixels and assigning the hit to the pixel receiving the highest fraction of the total charge [21,27,28].

Multiple counts (detection or removal) and charge-sharing (level of correction) strongly influence the performance of a system in terms of spectral and spatial resolution, noise response and detection efficiency.

In this work, we characterized the Pixirad-1/Pixie-III XPCD device mounting a CdTe sensor. With a small pixel size of 62 μm, with high detection efficiency and a frame rate larger than 500 fps, this detection system is suitable for X-ray in vivo microtomography [29,30] and breast computed tomography [7]. Moreover, by implementing two energy thresholds, this system allows performing KES imaging with polychromatic sources [8,9].

It implements a pure counting mode and two specific modes that correct for the charge-sharing effect.

We studied how the different modes affect the energy resolution and/or determine imaging features. In particular, by varying the threshold and by switching among the acquisition modes, we measured:

- Energy resolution
- Spatial resolution
- Noise response
- Noise Equivalent Number of Quanta

2. Materials

2.1. Detection system

Pixirad-1/Pixie-III has a hybrid architecture made by coupling, with the flip-chip bonding technique, a high Z sensor with an application specific integrated circuit (ASIC) [24].

The sensor is a Schottky type diode array made of a 650 μm thick CdTe semiconductor with electron collection on the pixels. For each pixel the readout has two 15-bit counters fed by two independent discriminators with tunable energy thresholds.

Pixie-III is a CMOS ASIC with an active area of 3.17×2.49 cm^2 covered by a 512×402 matrix of square pixels with 62 μm pitch.

The ASIC implements three acquisition modes:

- Pixel Mode (**PM**): each pixel counts independently from the others.
- Neighbor Pixel Inhibit mode (**NPI**): only one counter per event is enabled. When the charge cloud spreads over multiple pixels, the NPI mode assigns the count to the pixel receiving the highest fraction of the total charge.
- Neighbor Pixel Inhibit and Pixel Summing Mode (**NPISUM**): the total energy of one event involving up to 4 neighboring pixels is evaluated by summing the signals of these 4 pixels. The recovered charge is converted to voltage and then discriminated against the threshold to assign the hit to a unique pixel, i.e. the one receiving the highest fraction of the total charge.

In addition to charge sharing, when energies above Cd or Te K-edges ($E_{K(Cd)} = 26.7$ keV and $E_{K(Te)} = 31.8$ keV) are employed, this device exhibits the emission of fluorescence photons (with energies $E_{Cd} = 23.1$ keV and $E_{Te} = 27.4$ keV) from Cd and Te. Fluorescence photons can also induce multiple counts that cannot be corrected as done for the charge-sharing effect. Thus, the overall performance of this detection system differs for energies below and above Cd and Te K-edges.

The response of the detection system is linear up to 10^5 $photons\ pixel^{-1}s^{-1}$ ($\approx 2.6 \cdot 10^7$ $photons\ mm^{-2}s^{-1}$). All the measurements have been performed in the linearity range of the detection system by setting fluence rates lower than $2 \cdot 10^6$ $photons\ mm^{-2}s^{-1}$.

During the acquisitions the detection system was cooled down to −30 °C and the CdTe crystal was biased with a working voltage of 400 V.

To avoid time-dependent artifacts due to long polarization times of the CdTe crystal [31,32], short data acquisitions have been planned. The longest acquisition time was as long as 10 s, consisting in the acquisition of 100 frames each with an exposure time of 100 ms.

2.2. Source

The data have been acquired at the biomedical beamline ID17 of the European Synchrotron Radiation Facility (ESRF, Grenoble, France).

The source is a 21-pole wiggler, placed 150 m upstream of the detection system. The beam, monochromatized by a double Silicon-bent Laue crystal, has a quasi-parallel geometry with divergence <1 mrad and <0.1 mrad respectively along the horizontal and the vertical directions and can reach a maximum size of 150×10 mm^2 ($H \times V$) [33]. The shape of the beam is flat along the horizontal direction and roughly Gaussian along the vertical direction.

At ID17, the beam can be shaped by three different remotely controlled slits systems installed at different distances from the source.

In this work, the beam size has been chosen to cover the entire horizontal length of the detector; in the vertical direction, the slits have been opened to have a beam height of 6.6 mm at the detector position.

The storage ring worked in top up mode (injections every hour), with a 2.5% maximum current difference; during the acquisitions, the current of the ring has been constantly monitored. For a fixed energy, all the acquisitions have been performed with similar ring currents to limit variations of fluence rate below 1%.

3. Methods

3.1. Energy resolution

The energy resolution is defined as the ratio between the full width half maximum (FWHM) of a peak in the differential spectrum and its energy [34]:

$$\frac{\Delta E}{E} = \frac{FWHM}{E} \tag{1}$$

In this work, the differential spectra have been obtained by acquiring and differentiating the integral spectra. These integral spectra have been recorded through a threshold scan, i.e. by moving the threshold *Thr* at steps of 0.5 keV at fixed beam energy and fluence. For each value of *Thr*, 50 images of the beam with an exposure time of 100 *ms* have been recorded and then summed. The integral spectrum has been obtained by plotting the average signal, measured in a fixed 450×30 *pixel* region of interest (ROI), against *Thr*. The ROI has been chosen to take the biggest area avoiding dead/hot pixels and inhomogeneities of the beam. In particular, the height of the ROI was the FWHM of the vertical (broadly Gaussian) shape of the beam. This choice allowed to take into account only the most intense part of the beam excluding the inhomogeneities of the beam along the tails.

The measured energy resolution depends on the properties of the CdTe crystal, the source and the electronics. When measured over several pixels, as in this work, the energy resolution is further degraded by the slight offset of threshold of the different pixels [14].

The measurements have been performed for photons with energies close to the K-edges of the contrast agents of interest in KES imaging such as e.g. Ag (25.52 keV), I (33.17 keV), Xe (34.56 keV), Ba (37.44 keV) and Gd (50.24 keV), i.e. 26 keV, 33 keV, 37 keV and 50 keV. For each energy, the energy spread of the beam was estimated in 116 eV, 187 eV, 235 eV and 429 eV (combined energy spread given by the beam divergence and the intrinsic Darwin curve of the crystals) [33].

3.2. Imaging features measurement

The characterization of the imaging features of the detection system have been carried out by using objective metrics. The spatial resolution has been evaluated by means of the presampling Line Spread Function (LSF) in the spatial domain and the presampling MTF in the frequency domain; the noise response has been evaluated in the frequency domain by using the NNPS [35,36]. To globally compare the imaging performance in different modes and with different discriminator thresholds we used the Noise Equivalent number of Quanta (NEQ) as described in Section 3.2.4.

Since MTF and NNPS measurements assume a homogeneous beam, the images have been processed with the flat field correction procedure, as explained in Di Trapani et al. [37]. In the present work, for each combination of energy, threshold and acquisition mode, the matrix employed for the flat field correction has been obtained by averaging 100 images of the beam.

At fixed energy and fluence rate, we compared the global imaging performance of different settings through the $NEQ(u)$; in this part of the study we used two energies 26 keV and 33 keV. These two energies have been chosen within the energy range [22 keV–34 keV] recommended to perform breast computed tomography [38,39].

3.2.1. Spatial resolution

The presampling LSFs have been measured by using the slanted edge method proposed by Samei et al. [40]. It consists in the acquisition of images of a thick absorber with a sharp edge placed near the detection system and slanted by a small angle with respect to the pixels; the digital images of the edge are then processed to obtain the presampling LSF.

The presampling MTF has been obtained from the 1D FFT (Fast Fourier Transform) of the LSF normalized to the MTF at zero frequency ($MTF(0)$).

To study the dependence of the spatial resolution on the threshold, the latter has been scanned at steps of 2 keV; this operation has been repeated for each of the three acquisition modes. For each value of the threshold we acquired 100 images of a slanted edge and averaged them.

The performance under the different conditions have been studied in both spatial and frequency domains by plotting respectively the FWHM of the LSF and the MTF 50% (i.e. the frequency for which $MTF = 0.5$) against Thr.

3.2.2. Noise response

The NNPS has been determined by analyzing the white field images acquired with threshold scans as done for the measurement of the spatial resolution. For the 2D NNPS we selected 1600 (59×59 $pixel$) sub-ROIs which overlap for half of their area horizontally.

To calculate the NNPS we then employed the following algorithm [41]:

$$NNPS(u,v) = \frac{\Delta x \Delta y}{N_x N_y M} \sum_{i=1}^{M} \frac{|FFT_{2D}(I_i(x,y) - \bar{I}_i)|^2}{\bar{Q}^2} \tag{2}$$

where u and v are the horizontal and vertical axes of the frequency domain, $I_i(x,y)$ is the ith sub ROI, $\bar{I}_i$ the average signal of the ith sub-ROI, $\bar{Q}^2$ the square of the average recorded signal, M the total number of ROIs, Δx, Δy the pixel sides and N_x, N_y the number of pixels of the ROI along horizontal and vertical directions.

The uncertainty of each data point of the $NNPS(u,v)$ has been quantified as the standard deviation of the average of the M realizations used for the measure of the NNPS with the Eq. (2).

The NNPS describes the correlation between different pixels allowing to study the cross-talk induced by multiple counts in neighboring pixels. In particular the presence of correlation between neighboring pixels acts as a low-pass filter shaping the NNPS [18]. Thus, the NNPS magnitude is expected to decrease with the increase of the frequency when a bigger fraction of multiple counts is recorded.

Since the data points of the 2D NNPS along the axes ($u = 0$ mm^{-1} and $v = 0$ mm^{-1}) can have higher values which are not representative of the stochastic noise [41], the 1D NNPS has been evaluated from the measured $NNPS(u,v)$ omitting the axes. The 1D NNPSs profiles were extracted from the 2D NNPS by adapting the procedure explained by the IEC-62220-1 [42] to our experimental conditions. In particular, horizontal and vertical 1D NNPSs profiles were obtained by averaging the data points from one row just above and below the axes $v = 0$ mm^{-1} ($NNPS_x$) and $u = 0$ mm^{-1} ($NNPS_y$). Each data point of $NNPS_x$ and $NNPS_y$ was associated with the frequency $f = \sqrt{u^2 + v^2}$. Finally we averaged the two profiles $NNPS_x$ and $NNPS_y$ to obtain a smoothed 1D NNPS profile.

3.2.3. Aliasing

A digital imaging system with a pixel pitch of Δx is characterized by its Nyquist frequency $f_{Ny} = 1/(2\Delta x)$, that is the maximum frequency which can be correctly sampled without incurring in aliasing [41].

Since the presampling MTF is the response of the system to a sinusoidal input before the stage of sampling, all the components of MTF with frequency higher than f_{Ny} are aliased in the sampled image.

For a pixellated detection system the $NNPS$ is proportional to the MTF^2 [36]. Thus, when aliasing occurs, the components of the presampling NNPS above f_{Ny} are folded back and overlap with those below f_{Ny} increasing the high frequency components of the NNPS measured on sampled images [41,43]. In these cases, the NNPS directly measured on digital images is flattened respect to the presampling NNPS.

For a XPCD, multiple counts act as a low-pass filter reducing the high frequency components of the signal. This means that when the system is undersampled multiple counts can limit the aliasing effects on noise by reducing the magnitude of the signal components above f_{Ny}.

3.2.4. Noise equivalent number of quanta

The global imaging performance of a detection system are the result of a compromise between spatial resolution and noise. For instance, if a physical phenomenon (such the charge sharing) induces a blur during the detection process, the noise decreases at the cost of a worsening of spatial resolution.

The NEQ measures the square of the Signal to Noise Ratio (SNR) in the frequency domain and it is defined as follows [41]:

$$NEQ(u) = \frac{MTF^2(u)}{NNPS(u)} \tag{3}$$

By quantifying, for each frequency, how the spatial resolution is impaired by the noise response, the NEQ stands as the optimal metrics to directly compare the overall imaging performance of a detection system under different acquisition settings.

NEQ has been calculated from the presampling 1D MTF and from the measured 1D NNPS and studied as a function of the threshold.

4. Results

4.1. Energy resolution

In Fig. 1 we report the differential spectra obtained with the monochromatic beam set to 26 keV, 33 keV, 37 keV and 50 keV.

Fig. 1(a) shows that, for the beam energy $E = 26$ keV ($E < E_{K(Cd)}$), the spectra depend only on the acquisition modes as follows:

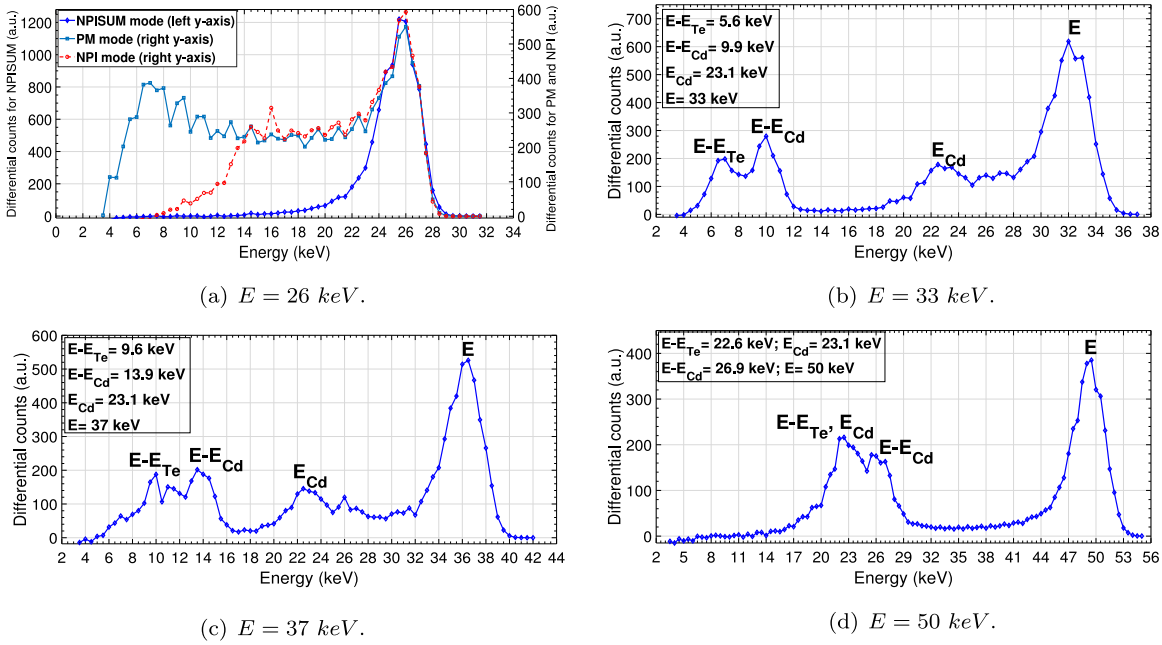

(a) $E = 26\ keV$. (b) $E = 33\ keV$.

(c) $E = 37\ keV$. (d) $E = 50\ keV$.

Fig. 1. Differential spectra for: (a) $E = 26$ keV (PM and NPI right y axis; NPISUM left y axis); (b) $E = 33$ keV (NPISUM); (c) $E = 37$ keV (NPISUM); (d) $E = 50$ keV (NPISUM).

Table 1
FWHM (keV) and energy resolution measured on the full energy peak.

Energy (keV)	FWHM (keV)	$\Delta E/E$
26	3.4 ± 0.4	$(13 \pm 2)\%$
33	3.6 ± 0.4	$(11 \pm 1)\%$
37	3.7 ± 0.4	$(10 \pm 1)\%$
50	4.1 ± 0.4	$(8.2 \pm 0.8)\%$

- **NPISUM** mode recovers the charge spread, no multiple counts are recorded and the differential spectrum shows only one peak corresponding to the energy of the impinging photons (i.e. the full energy peak). The comparison with PM and NPI modes shows that the NPISUM mode achieves the highest number of counts in the full energy peak. This means that, if compared to the other modes, NPISUM mode preserves the detection efficiency when a high threshold is set.
- **PM** mode does not remove multiple counts. The spectrum shows a not resolved full energy peak with a long left tail, according to Vincenzi et al. [14].
- **NPI** mode removes multiple counts, but does not recover the spread of the charge. This means that for $Thr > E/2$ there is a loss of detection efficiency depending on the threshold value. As a consequence, the spectrum shows a not completely resolved full energy peak with asymmetric tails.

All the spectra in Figs. 1(b) (c) and (d), obtained using energies above the Cd and Te K-edges, show additional signals due to fluorescence and escape peaks corresponding to $E_{Cd} = 23.1$ keV and E–E_{Cd}, E–E_{Te} respectively. The Te fluorescence photons do not produce a signal in the differential spectra at $E_{Te} = 27.4$ keV because, having an energy just above the Cd K-edge, in CdTe they have a mean free path ($\lambda_{Te} = 61.6$ μm) comparable with the pixel size. For this reason, the re-absorption of the Te fluorescence photon is highly probable within the same range in which charge sharing occurs.

In Table 1 we report both the FWHM and the energy resolution for the NPISUM mode at all the beam energies here considered.

4.2. Spatial resolution

Fig. 2 shows the plots of the FWHM of the presampling LSFs and MTF 50% against the threshold Thr for the beam energy $E = 26$ keV.

The results can be summarized as follows:

- NPISUM mode: no multiple counts are recorded; both FWHM and MTF 50% are almost independent from the applied Thr. Moreover, the FWHM of the LSF has a size of 64 μm, comparable with that of the pixel pitch 62 μm.
- PM mode: the spatial resolution improves by increasing Thr; the FWHM and MTF 50% respectively decreases and increases with Thr. In particular for $Thr < E/2$ the FWHM is larger than the pixel size, for $Thr > E/2$ there is a reduction of the effective pixel size that improves the spatial resolution in agreement with Marchal and Medjoubi [18], Lopez et al. [17] and Delogu et al. [10].
- NPI mode: for $Thr < E/2$, thanks to the removal of multiple counts the NPI mode shows the same behavior of the NPISUM mode. For $Thr > E/2$ the spatial resolution improves as observed for the PM mode.

Fig. 3 shows the plots of the FWHM of the presampling LSFs and of MTF 50% against the threshold Thr for the beam energy $E = 33$ keV. The behavior of the acquisition modes can be described as follows:

- the NPISUM shows almost constant FWHM and MTF 50% values up to $Thr \leq E_{Cd}$. For $Thr > E_{Cd}$ the fluorescence photons are totally removed inducing an improvement of the spatial resolution. In particular, with respect of $Thr = 22$ keV, the MTF 50% increases from a minimum of 10% ($Thr = 24$ keV) to a maximum of 36% ($Thr = 30$ keV).
- in PM mode, the spatial resolution improves with the increase of Thr. In particular, for $Thr < E/2$ the PM mode has a lower spatial resolution if compared to NPISUM mode. For $Thr > E/2$ the FWHM decreases to values below the true aperture of 62 μm, in agreement with the behavior at 26 keV.
- the NPI mode shows roughly the same performance of the NPISUM mode for $Thr < E/2$ and the same performance of PM mode for $Thr > E/2$.

Fig. 4 compares the presampling MTF obtained with PM and NPISUM modes coupled with two representative thresholds (one below and one above E/2) for the two energies (a) 26 keV and (b) 33 keV. In Fig. 4 the Nyquist frequency (f_{Ny}) and the aperture function have been represented as reference. The aperture function is given by $|sinc(\pi \cdot u \cdot \Delta x)|$ and it is the Fourier transform of the ideal aperture for a square pixel

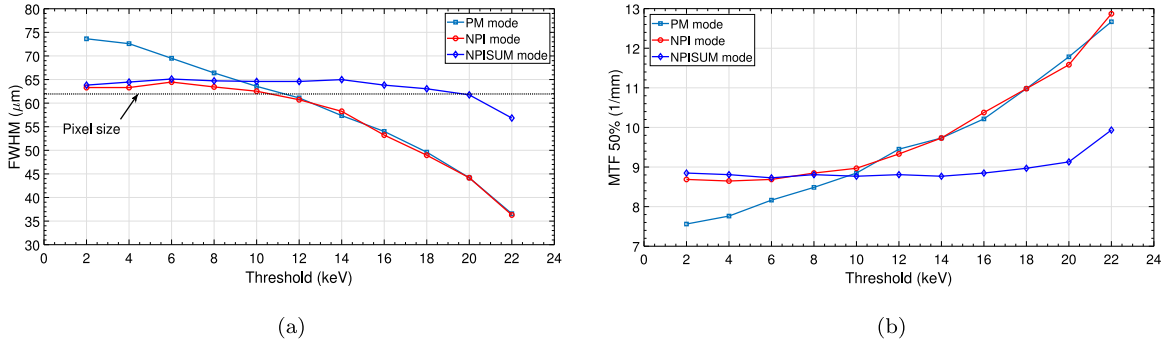

Fig. 2. $E = 26$ keV: (a) plot of FWHM of the Line Spread Function against the threshold; (b) MTF 50% against the threshold.

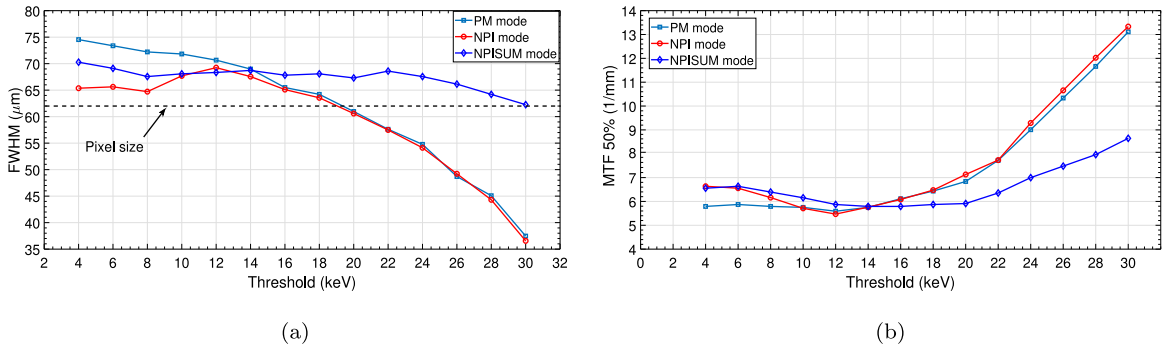

Fig. 3. $E = 33$ keV: (a) plot of FWHM of the Line Spread Function against the threshold; (b) MTF 50% against the threshold.

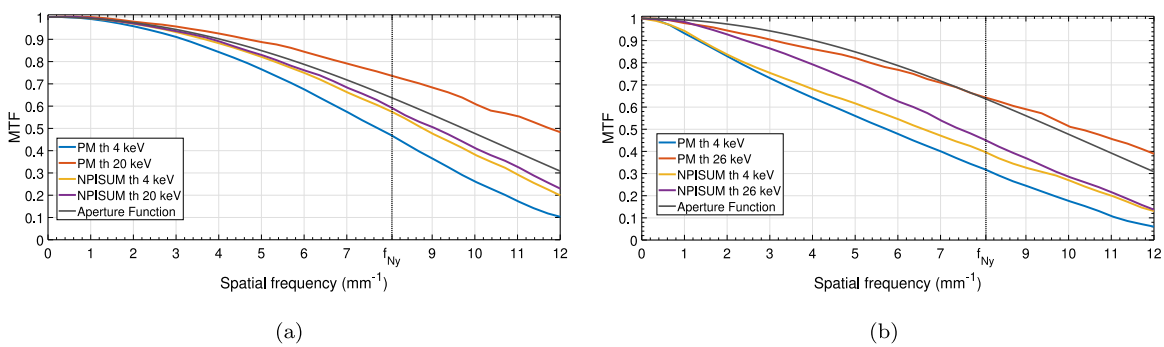

Fig. 4. Comparison of MTFs response for the two energies (a) 26 keV and (b) 33 keV for PM and NPISUM modes and different thresholds.

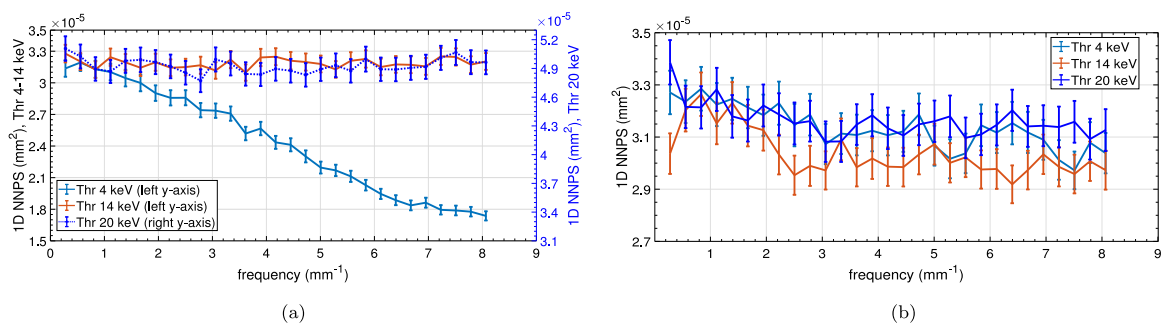

Fig. 5. 1D NNPS response for different thresholds with monochromatic beam $E = 26$ keV: (a) PM mode; (b) NPISUM mode.

with side Δx. By comparing Fig. 4 (a) and (b), it appears clear how, at fixed threshold, the MTF values measured with $E = 33$ keV are lower than those measured with $E = 26$ keV. This worsening of the spatial resolution involves both PM and NPISUM modes and it is due to Cd-emitted fluorescence photons that, having a mean free path of $\lambda_{Cd} = 124$ μm in CdTe, play a major role in the spatial resolution degradation if compared to the effects due to charge sharing. Fig. 4 shows also that for each combination of mode, energy and thresholds the MTF extends above the Nyquist frequency, thus the system is always undersampled.

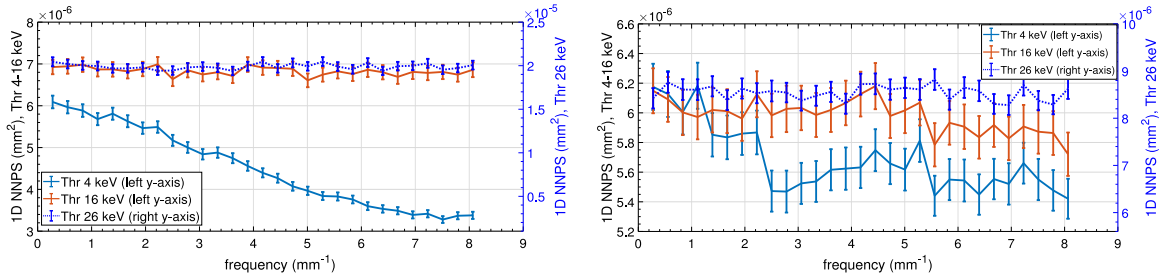

Fig. 6. 1D NNPS response for different thresholds using monochromatic beam $E = 33$ keV. (a) PM mode; (b) NPISUM mode.

4.3. Noise response

The plots of 1D NNPS for monochromatic photons at $E = 26$ keV for few threshold values are reported in Fig. 5(a) and (b) for PM and NPISUM mode, respectively.

In PM mode:

- for $Thr = 4$ keV ($Thr < E/2$) multiple counts induce correlations between adjacent pixels acting as a low-pass filter that reduces the high frequency components of the $NNPS$.
- for $Thr = 14$ keV ($Thr \approx E/2$) multiple counts are totally removed and the NNPS is flat.
- for $Thr = 20$ keV ($Thr > E/2$) multiple counts are totally removed and the NNPS flat. The increase of NNPS magnitude is due to the loss of detection efficiency.

For NPISUM mode, the NNPS is quite flat with its magnitude independent from Thr (Fig. 5(b)).

Fig. 6(a) and (b) show the 1D NNPS for PM and for NPISUM modes respectively, for photons with $E = 33$ keV.

For $Thr = 4$ keV ($< E_{Cd}/2$), the low-pass filtering effect on the 1D NNPSs is visible for both modes: in NPISUM mode it depends on Cd-emitted fluorescence photons; in PM mode it is due to multiple counting both from charge sharing and from fluorescence photons. By increasing the threshold to $Thr > E/2$ the 1D NNPS flattens for both modes. The increase of the 1D NNPS in PM mode for $Thr = 26$ keV can be explained in terms of loss of efficiency. This effect occurs also in NPISUM mode for $Thr \geq 26$ keV when fluorescence photons are not recorded.

4.4. Aliasing

Fig. 4 shows that for all the settings the presampling MTF extents above the Nyquist frequency. This implies that the system is always undersampled and aliasing occurs.

Aliasing increases the high frequency components of noise, thus flattening the NNPS. Referring to Figs. 5 and 6, the flattening of the NNPS is enhanced when using settings which remove multiple counts, i.e. PM mode combined with $Thr > E/2$ or NPISUM mode for $E = 26$ keV and both PM and NPISUM modes combined with $Thr > E/2$ for $E = 33$ keV.

The effect of the detection or removal of multiple counts on both NNPS and presampling MTF can be summarized as follows:

- multiple counts detection worsens the presampling MTF and reduces the high frequency components of the NNPS. Moreover, working as a low-pass filtering in the stage before the sampling, it prevents aliasing effects such the flattening of the NNPS.
- multiple counts removal improves the spatial resolution but increases the high frequency components of the NNPS. The improvement of the spatial resolution leads to an increase of the magnitude of the presampling MTF components above f_{Ny}, thus aliasing effects are increased too.

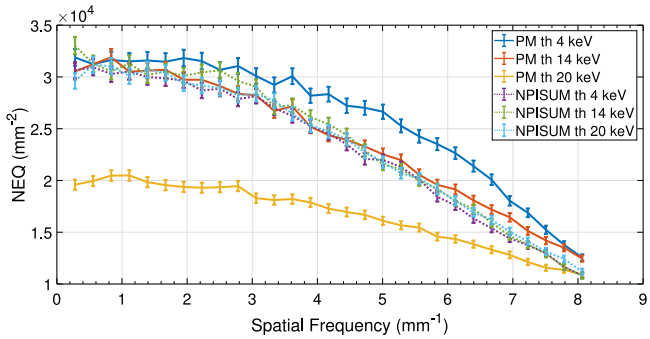

Fig. 7. $E = 26$ keV NEQ response of PM Vs NPISUM mode.

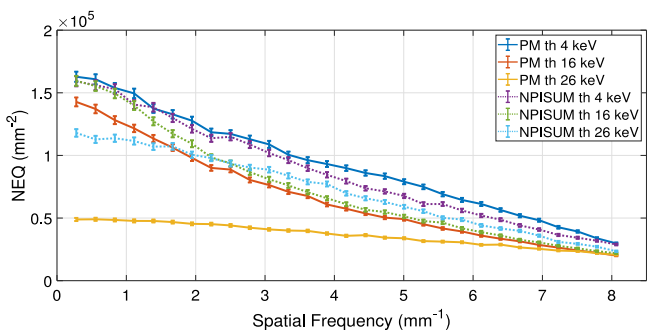

Fig. 8. $E = 33$ keV: NEQ response of PM Vs NPISUM mode.

4.5. Noise equivalent number of quanta

Fig. 7 shows the NEQ calculated in PM and NPISUM modes for the energy $E = 26$ keV.

The results can be summarized as follows:

- in the NPISUM mode the NEQ is almost independent from the threshold.
- in the PM mode the NEQ values decrease at all frequencies with the increase of the threshold. In particular, for $Thr = 20$ keV there is a drop in the NEQ explainable with the loss of detection efficiency.

The plots of NEQ for the beam $E = 33$ keV are reported in Fig. 8.

The behavior of the two modes when using different thresholds can be described in this way:

- in the NPISUM mode, for spatial frequencies < 2.2 mm^{-1}, the NEQ always decreases by increasing the threshold. For frequencies > 2.2 mm^{-1} the NEQ at $Thr = 26$ keV is higher with respect to that measured for $Thr = 16$ keV. This behavior is due to the fact that fluorescence photons detection (possible for $Thr < E_{Cd} = 23.1$ keV) preserves the efficiency, but increases the noise

(i.e. increases the NNPS) and worsens the MTF especially at high frequencies. In terms of NEQ, this means that, by discriminating fluorescence photons $Thr = 26$ keV is more effective than $Thr = 16$ keV in resolving spatial frequencies > 2.2 mm^{-1}.

- in the PM mode the NEQ response always decreases when increasing the threshold.

For both energies the combination of the PM mode with low thresholds shows the best NEQ response, i.e. the highest NEQ values at all frequencies.

5. Discussion and conclusions

A systematic study on the Pixirad-1/Pixie-III XPCD has been performed by considering different acquisition modes and threshold values.

The measurement of the energy resolution demonstrated that only the NPISUM mode allows for a full energy resolution and, in the range [26 keV–50 keV], the energy resolution of NPISUM mode varies from 13% to 8.2%.

The spatial resolution measurements showed that the performance strongly depends on the fraction of multiple counts recorded when charge sharing is not corrected: presampling LSF and MTF improve when high threshold values are set. Instead, the NPISUM mode, which fully corrects the charge-sharing effects, allows an almost threshold independent spatial resolution. More in general, for all the acquisition thresholds, the system achieve a LSF with $FWHM < 75$ μm (at $E \leq 33$ keV). This feature makes this system suitable for in vivo microtomography [29,30] and for breast imaging by allowing the resolution of breast micro-calcifications with typical diameters < 0.5 mm [44].

The analysis of the noise response confirmed that a higher fraction of multiple counts detection decreases the noise by reducing the high frequency components of the NNPS.

We observed that the system is always undersampled. However, by acting as a low-pass filter, the detection of multiple counts brings the system close to the condition of optimal sampling as described in sect. Section 3.2.3 and thus, it reduces aliasing effects on noise.

The results of the comparison among the overall imaging performance with different acquisition settings, conducted through NEQ can be summarized as follows:

- the highest NEQ values are achieved by using the PM mode in combination with low thresholds. This means that the NEQ response is improved as more multiple counts are detected.
- for higher thresholds (in particular for $Thr > E/2$), the NPISUM mode shows a better NEQ response than the PM mode.

The comparison of the NEQ curves can be a useful tool to guide the choice of the optimal combination of acquisition mode and operating threshold according to the specific application. In particular, to perform imaging requiring both a good energy resolution and the use of high threshold values, which are common condition in spectral imaging, the NPISUM mode has to be preferred to the PM mode. This conclusion is in line with the findings in [8,9,45,46] where the benefits of the charge sharing correction on spectral imaging have been proved by using respectively Pixirad/Pixie-III and Medipix3 based detection systems.

For other imaging applications, in which a good energy resolution is not mandatory, multiple counts from charge sharing and fluorescence can improve the NEQ response by reducing the global noise and the aliasing effects. In such cases, the pure counting mode and low threshold values have to be preferred. This conclusion, here verified for the Pixirad-1/Pixie-III, can be extended to other XPCD devices with similar features.

Declaration of competing interest

The authors declare that they have no known competing financial interests or personal relationships that could have appeared to influence the work reported in this paper.

CRediT authorship contribution statement

V. Di Trapani: Conceptualization, Methodology, Data curation, Formal analysis, Investigation, Validation, Writing - original draft, Writing - review & editing. **A. Bravin:** Investigation, Validation, Writing - review & editing. **F. Brun:** Funding acquisition, Investigation, Validation, Writing - review & editing. **D. Dreossi:** Validation, Writing - review & editing. **R. Longo:** Validation, Writing - review & editing. **A. Mittone:** Investigation, Validation, Writing - review & editing. **L. Rigon:** Validation, Writing - review & editing. **P. Delogu:** Formal analysis, Investigation, Supervision, Validation, Writing - original draft, Writing - review & editing.

Acknowledgments

This work was conducted within the KEST (K-Edge Subtraction Tomography) project, which is funded by Istituto Nazionale di Fisica Nucleare, Italy (National Scientific Committee 5 for Technological and Inter-Disciplinary research).

Authors wish to thank the ESRF for the provision of the beamtime MI 1323, and Dr. H. Requardt for his support during data acquisition at ID17 ESRF. This study was supported by the Swedish Research Council, Sweden (grant no. X2015-99x-22731-01-4) and by the COST Action CA16122 BIONECA.

References

[1] D. Pacella, Energy-resolved x-ray detectors: The future of diagnostic imaging, Rep. Med. Imag. 8 (2015) 1, http://dx.doi.org/10.2147/RMI.S50045.

[2] K. Taguchi, J.S. Iwanczyk, Vision 20/20: Single photon counting x-ray detectors in medical imaging, Medical Physics 40 (10) (2013) 100901, http://dx.doi.org/10.1118/1.4820371.

[3] S. Weigel, S. Berkemeyer, R. Girnus, A. Sommer, H. Lenzen, W. Heindel, Digital mammography screening with photon-counting technique: can a high diagnostic performance be realized at low mean glandular dose? Radiology 271 (2) (2014) 345–355, http://dx.doi.org/10.1148/radiol.13131181.

[4] N. Berger, M. Marcon, N. Saltybaeva, W. A Kalender, H. Alkadhi, T. Frauenfelder, A. Boss, Dedicated breast computed tomography with a photon-counting detector: initial results of clinical in vivo imaging, Investigative Radiol. 54 (7) (2019) 409–418, http://dx.doi.org/10.1097/RLI.0000000000000552.

[5] P. Delogu, B. Golosio, C. Fedon, F. Arfelli, R. Bellazzini, A. Brez, F. Brun, F.D. Lillo, D. Dreossi, G. Mettivier, M. Minuti, P. Oliva, M. Pichera, L. Rigon, P. Russo, A. Sarno, G. Spandre, G. Tromba, R. Longo, Imaging study of a phase-sensitive breast-CT system in continuous acquisition mode, J. Instrum. 12 (01) (2017) C01016, http://dx.doi.org/10.1088/1748-0221/12/01/c01016.

[6] L. Brombal, S. Donato, F. Brun, P. Delogu, V. Fanti, P. Oliva, L. Rigon, V. Di Trapani, R. Longo, B. Golosio, Large-area single-photon-counting CdTe detector for synchrotron radiation computed tomography: a dedicated preprocessing procedure, J. Synchrotron Radiat. 25 (4) (2018) 1068–1077, http://dx.doi.org/10.1107/S1600577518006197.

[7] R. Longo, F. Arfelli, D. Bonazza, U. Bottigli, L. Brombal, A. Contillo, M.A. Cova, P. Delogu, F.D. Lillo, V. Di Trapani, S. Donato, D. Dreossi, V. Fanti, C. Fedon, B. Golosio, G. Mettivier, P. Oliva, S. Pacile, A. Sarno, L. Rigon, P. Russo, A. Taibi, M. Tonutti, F. Zanconati, G. Tromba, Advancement in phase-contrast breast CT using monochromatic beam, J. Synchrotron Radiat. 26 (4) (2019) 1343–1353, http://dx.doi.org/10.1107/S1600577519005502.

[8] F. Brun, V. Di Trapani, D. Dreossi, R. Longo, P. Delogu, L. Rigon, K-edge spectral computed tomography with a photon counting detector and discrete reconstruction, in: 2018 40th Annual International Conference of the IEEE Engineering in Medicine and Biology Society (EMBC), 2018, pp. 5245–5248, http://dx.doi.org/10.1109/EMBC.2018.8513425.

[9] F. Brun, V. Di Trapani, D. Dreossi, L. Rigon, R. Longo, P. Delogu, Towards in vivo K-edge X-ray micro-CT with the pixirad-I/pixie-III detector, in: L. Lhotska, L. Sukupova, I. Lacković, G.S. Ibbott (Eds.), World Congress on Medical Physics and Biomedical Engineering 2018, Springer Singapore, Singapore, 2019, pp. 123–126, http://dx.doi.org/10.1007/978-981-10-9035-6_22.

[10] P. Delogu, P. Oliva, R. Bellazzini, A. Brez, P. de Ruvo, M. Minuti, M. Pinchera, G. Spandre, A. Vincenzi, Characterization of Pixirad-1 photon counting detector for X-ray imaging, J. Instrum. 11 (01) (2016) P01015, http://dx.doi.org/10.1088/1748-0221/11/01/p01015.

[11] G. Pellegrini, M. Chmeissani, M. Maiorino, G. Blanchot, J. Garcia, M. Lozano, R. Martinez, C. Puigdengoles, M. Ullan, P. Casado, Performance limits of a 55-/spl mu/m pixel CdTe detector, IEEE Trans. Nucl. Sci. 53 (1) (2006) 361–366, http://dx.doi.org/10.1109/TNS.2006.869843.

[12] E. Guni, J. Durst, B. Kreisler, T. Michel, G. Anton, M. Fiederle, A. Fauler, A. Zwerger, The influence of pixel pitch and electrode pad size on the spectroscopic performance of a photon counting pixel detector with CdTe sensor, IEEE Trans. Nucl. Sci. 58 (1) (2011) 17–25, http://dx.doi.org/10.1109/TNS.2010.2095883.
[13] M. Veale, S. Bell, D. Duarte, A. Schneider, P. Seller, M. Wilson, K. Iniewski, Measurements of charge sharing in small pixel CdTe detectors, Nucl. Instrum. Methods Phys. Res. A 767 (2014) 218–226, http://dx.doi.org/10.1016/j.nima.2014.08.036.
[14] A. Vincenzi, P.D. Ruvo, P. Delogu, R. Bellazzini, A. Brez, M. Minuti, M. Pinchera, G. Spandre, Energy characterization of Pixirad-1 photon counting detector system, J. Instrum. 10 (04) (2015) C04010, http://dx.doi.org/10.1088/1748-0221/10/04/c04010.
[15] P. Zambon, V. Radicci, P. Trueb, C. Disch, M. Rissi, T. Sakhelashvili, M. Schneebeli, C. Broennimann, Spectral response characterization of CdTe sensors of different pixel size with the IBEX ASIC, Nucl. Instrum. Methods Phys. Res. A 892 (2018) 106–113, http://dx.doi.org/10.1016/j.nima.2018.03.006.
[16] E.N. Gimenez, R. Ballabriga, M. Campbell, I. Horswell, X. Llopart, J. Marchal, K.J.S. Sawhney, N. Tartoni, D. Turecek, Study of charge-sharing in MEDIPIX3 using a micro-focused synchrotron beam, J. Instrum. 6 (01) (2011) C01031, http://dx.doi.org/10.1088/1748-0221/6/01/c01031.
[17] F.C.M. Lopez, L. Rigon, L. Fardin, F. Arfelli, A. Bergamaschi, D. Dreossi, M. Longo, B. Schmitt, E. Vallazza, R. Longo, Comparator threshold settings and the effective pixel width of the PICASSO detector, J. Instrum. 9 (05) (2014) C05056, http://dx.doi.org/10.1088/1748-0221/9/05/c05056.
[18] J. Marchal, K. Medjoubi, Detective quantum efficiency model of single-X-ray-photon counting hybrid pixel detectors, J. Instrum. 7 (2012) P11028, http://dx.doi.org/10.1088/1748-0221/7/11/P11028.
[19] C. Broennimann, E.F. Eikenberry, B. Henrich, R. Horisberger, G. Huelsen, E. Pohl, B. Schmitt, C. Schulze-Briese, M. Suzuki, T. Tomizaki, H. Toyokawa, A. Wagner, The PILATUS 1M detector, J. Synchrotron Radiat. 13 (2) (2006) 120–130, http://dx.doi.org/10.1107/S0909049505038665.
[20] K. Mathieson, M. Passmore, P. Seller, M. Prydderch, V. O'Shea, R. Bates, K. Smith, M. Rahman, Charge sharing in silicon pixel detectors, Nucl. Instrum. Methods Phys. Res. A 487 (1) (2002) 113–122, http://dx.doi.org/10.1016/S0168-9002(02)00954-3, 3rd International Workshop on Radiation Imaging Detectors.
[21] X. Llopart, M. Campbell, R. Dinapoli, D. San Segundo, E. Pernigotti, Medipix2: A 64-k pixel readout chip with 55-/spl mu/m square elements working in single photon counting mode, IEEE Trans. Nucl. Sci. 49 (5) (2002) 2279–2283, http://dx.doi.org/10.1109/TNS.2002.803788.
[22] L. Rossi, P. Fischer, T. Rohe, N. Wermes, Pixel Detectors: From Fundamentals to Applications, Springer Berlin Heidelberg, Berlin, Heidelberg, 2006, http://dx.doi.org/10.1007/3-540-28333-1.
[23] C. Ullberg, M. Urech, N. Weber, A. Engman, A. Redz, F. Henckel, Measurements of a dual-energy fast photon counting CdTe detector with integrated charge sharing correction, Proc. SPIE 8668 (2013) http://dx.doi.org/10.1117/12.2007892.
[24] R. Bellazzini, A. Brez, G. Spandre, M. Minuti, M. Pinchera, P. Delogu, P. de Ruvo, A. Vincenzi, PIXIE III: a very large area photon-counting CMOS pixel ASIC for sharp X-ray spectral imaging, J. Instrum. 10 (01) (2015) C01032, http://dx.doi.org/10.1088/1748-0221/10/01/c01032.
[25] P. Maj, P. Grybos, R. Szczygiel, P. Kmon, R. Kleczek, A. Drozd, P. Otfinowski, G. Deptuch, Measurements of matching and noise performance of a prototype readout chip in 40 nm CMOS process for hybrid pixel detectors, IEEE Trans. Nucl. Sci. 62 (1) (2015) 359–367, http://dx.doi.org/10.1109/TNS.2014.2385595.
[26] R. Ballabriga, J. Alozy, M. Campbell, E. Frojdh, E. Heijne, T. Koenig, X. Llopart, J. Marchal, D. Pennicard, T. Poikela, L. Tlustos, P. Valerio, W. Wong, M. Zuber, Review of hybrid pixel detector readout ASICs for spectroscopic X-ray imaging, J. Instrum. 11 (01) (2016) P01007, http://dx.doi.org/10.1088/1748-0221/11/01/p01007.
[27] H.-E. Nilsson, B. Norlin, C. Fröjdh, L. Tlustos, Charge sharing suppression using pixel-to-pixel communication in photon counting x-ray imaging systems, Nucl. Instrum. Methods Phys. Res. 576 (1) (2007) 243–247, http://dx.doi.org/10.1016/j.nima.2007.01.160, Proceedings of the 8th International Workshop on Radiation Imaging Detectors.
[28] P. Maj, A. Baumbaugh, G. Deptuch, P. Grybos, R. Szczygiel, Algorithms for minimization of charge sharing effects in a hybrid pixel detector taking into account hardware limitations in deep submicron technology, J. Instrum. 7 (12) (2012) C12020, http://dx.doi.org/10.1088/1748-0221/7/12/c12020.
[29] P. Coan, A. Wagner, A. Bravin, P. Diemoz, J. Keyrilainen, J. Mollenhauer, In vivo x-ray phase contrast analyzer-based imaging for longitudinal osteoarthritis studies in guinea pigs, Phys. Med. Biol. 55 (24) (2010) 7649–7662, http://dx.doi.org/10.1088/0031-9155/55/24/017.
[30] L. Broche, G. Perchiazzi, L. Porra, A. Tannoia, M. Pellegrini, S. Derosa, A. Sindaco, J. Borges, L. Degrugilliers, A. Larsson, G. Hedenstierna, A. Wexler, A. Bravin, S. Verbanck, B. Smith, J. Bates, S. Bayat, Dynamic mechanical interactions between neighboring airspaces determine cyclic opening and closure in injured lung, Critical Care Med. 45 (2017) http://dx.doi.org/10.1097/CCM.0000000000002234.
[31] P. Delogu, L. Brombal, V. Di Trapani, S. Donato, U. Bottigli, D. Dreossi, B. Golosio, P. Oliva, L. Rigon, R. Longo, Optimization of the equalization procedure for a single-photon counting CdTe detector used for CT, J. Instrum. 12 (11) (2017) C11014, http://dx.doi.org/10.1088/1748-0221/12/11/c11014.
[32] M. Ruat, C. Ponchut, Defect signature, instabilities and polarization in CdTe X-ray sensors with quasi-ohmic contacts, J. Instrum. 9 (04) (2014) C04030, http://dx.doi.org/10.1088/1748-0221/9/04/c04030.
[33] P. Suortti, S. Fiedler, A. Bravin, T. Brochard, M. Mattenet, M. Renier, P. Spanne, W. Thomlinson, A.M. Charvet, H. Elleaume, C. Schulze-Briese, A.C. Thompson, Fixed-exit monochromator for computed tomography with synchrotron radiation at energies 18–90keV, J. Synchrotron Radiat. 7 (5) (2000) 340–347, http://dx.doi.org/10.1107/S0909049500008384.
[34] G.F. Knoll, Radiation Detection and Measurement, fourth ed., Wiley New York, 2010.
[35] I.A. Cunningham, Applied linear-systems theory, in: R.L.V. Metter, J. Beutel, H.L. Kundel (Eds.), Handbook of Medical Imaging, Volume 1. Physics and Psychophysics, SPIE, Bellingham, WA, USA, 2000, pp. 79–160, http://dx.doi.org/10.1117/3.832716.ch2.
[36] W. Vennart, ICRU report 54: Medical imaging - the assessment of image quality: ISBN 0-913394-53-X. April 1996, Maryland, U.S.A., Radiography 3 (3) (1997) 243–244, http://dx.doi.org/10.1016/S1078-8174(97)90038-9.
[37] V. Di Trapani, A. Bravin, F. Brun, D. Dreossi, R. Longo, A. Mittone, L. Rigon, P. Delogu, Characterization of noise and efficiency of the Pixirad-1/Pixie-III CdTe X-ray imaging detector, J. Instrum. 13 (12) (2018) C12008, http://dx.doi.org/10.1088/1748-0221/13/12/c12008.
[38] M. Weigel, S.V. Vollmar, W.A. Kalender, Spectral optimization for dedicated breast CT, Med. Phys. 38 (1) (2011) 114–124, http://dx.doi.org/10.1118/1.3523599.
[39] P. Delogu, V. Di Trapani, L. Brombal, G. Mettivier, A. Taibi, P. Oliva, Optimization of the energy for Breast monochromatic absorption X-ray Computed Tomography, Sci. Rep. 9 (13135) (2019) http://dx.doi.org/10.1038/s41598-019-49351-2.
[40] E. Samei, M.J. Flynn, D.A. Reimann, A method for measuring the presampled MTF of digital radiographic systems using an edge test device, Med. Phys. 25 (1) (1998) 102–113, http://dx.doi.org/10.1118/1.598165.
[41] J.T. Dobbins, Image quality metrics for digital systems, in: R.L.V. Metter, J. Beutel, H.L. Kundel (Eds.), Handbook of Medical Imaging, Volume 1. Physics and Psychophysics, SPIE, Bellingham, WA, USA, 2000, pp. 161–222, http://dx.doi.org/10.1117/3.832716.ch3.
[42] International Electrotechnical Commission, Medical electrical equipment-Characteristics of digital X-ray imaging devices Part-1: determination of the detective quantum efficiency, IEC 62220-1 Geneva: IEC, 2003.
[43] M.L. Giger, K. Doi, Investigation of basic imaging properties in digital radiography. I. Modulation transfer function, Med. Phys. 11 (3) (1984) 287–295, http://dx.doi.org/10.1118/1.595629.
[44] P. Henrot, A. Leroux, C. Barlier, P. Genin, Breast microcalcifications: The lesions in anatomical pathology, Diagn. Interv. Imaging 95 (2) (2014) 141–152, http://dx.doi.org/10.1016/j.diii.2013.12.011, Radio-histological correlations in breast imaging.
[45] M.F. Walsh, A.M.T. Opie, J.P. Ronaldson, R.M.N. Doesburg, S.J. Nik, J.L. Mohr, R. Ballabriga, A.P.H. Butler, P.H. Butler, First CT using Medipix3 and the MARS-CT-3 spectral scanner, J. Instrum. 6 (01) (2011) C01095, http://dx.doi.org/10.1088/1748-0221/6/01/c01095.
[46] T. Koenig, M. Zuber, E. Hamann, A. Cecilia, R. Ballabriga, M. Campbell, M. Ruat, L. Tlustos, A. Fauler, M. Fiederle, T. Baumbach, How spectroscopic x-ray imaging benefits from inter-pixel communication, Phys. Med. Biol. 59 (20) (2014) 6195–6213, http://dx.doi.org/10.1088/0031-9155/59/20/6195.